3D-Structured Stretchable Strain Sensors for Out-of-Plane Force Detection

Zhiyuan Liu, Dianpeng Qi, Wan Ru Leow, Jiancan Yu, Michele Xiloyannnis, Leonardo Cappello, Yaqing Liu, Bowen Zhu, Ying Jiang, Geng Chen, Lorenzo Masia, Bo Liedberg, and Xiaodong Chen*

Stretchable strain sensors, as the soft mechanical interface, provide the key mechanical information of the systems for healthcare monitoring, rehabilitation assistance, soft exoskeletal devices, and soft robotics. Stretchable strain sensors based on 2D flat film have been widely developed to monitor the in-plane force applied within the plane where the sensor is placed. However, to comprehensively obtain the mechanical feedback, the capability to detect the out-of-plane force, caused by the interaction outside of the plane where the senor is located, is needed. Herein, a 3D-structured stretchable strain sensor is reported to monitor the out-of-plane force by employing 3D printing in conjunction with out-of-plane capillary force-assisted self-pinning of carbon nanotubes. The 3D-structured sensor possesses large stretchability, multistrain detection, and strain-direction recognition by one single sensor. It is demonstrated that out-of-plane forces induced by the air/fluid flow are reliably monitored and intricate flow details are clearly recorded. The development opens up for the exploration of next-generation 3D stretchable sensors for electronic skin and soft robotics.

Stretchable strain sensors are crucial for the soft mechanical interface to obtain the mechanical feedback for healthcare, rehabilitation monitoring, human–machine interaction, and soft robotics.[1–15] There are mainly two categories of the mechanical force interacting with the stretchable strain sensor: in-plane force and out-of-plane force (**Figure 1**a and Figure S1, Supporting Information). In-plane force is normally applied by direct stretching of the sensor, such as the tensile force induced by the skin deformation and joint bending, and the applied force is in the plane where the sensor is placed. 2D flat-film

stretchable strain sensors have been widely developed to detect such in-plane force by employing various of active materials, such as metal/carbon nanomaterials, conductive polymers, liquid metal, microfluidics, and so on.[2,16–52] Proper strategies were also proposed to enhance the sensitivity of the 2D sensor, and system-level design by assembling multiple flat-film sensors was developed to achieve motion recognition.[53] Out-of-plane force is caused by the interaction outside of the plane where the senor is located, for example, induced by the air/fluid flow, or other indirect contact to the sensor. Out-of-plane force detection can significantly enhance the capability of the system to perceive the environment, because the physical interaction with the external environment always involves the air/fluid flow. In fact, in nature, animals and plants, like spiders and Venus flytrap, have already evolved to possess the soft stretchable sensor to sense the mechanical signal induced by such out-of-plane force.[54–56] In contrast to the abundant research of the 2D flat-film stretchable strain sensor, a few nonstretchable 3D-structured strain sensors were fabricated based on new composite materials[57–59] and the delicate microelectromechanical systems technology[60–66] to detect the out-of-plane force. However, it remains a big challenge to design a 3D-structured stretchable strain sensor with optimized structures for sensitivity enhancement, high stretchability, and strain-direction recognition for the out-of-plane force detection.

Herein, we report a 3D-structured stretchable strain sensor composed of stretchable sensing units by employing a capillary force-assisted 3D self-pinning effect. Our 3D-structured stretchable strain sensors work excellently up to 120% tensile strain applied to the sensing unit. It is also capable of detecting multistrains and the corresponding strain direction by using one single sensor with good stability and repeatability (more than 10 000 strain cycles). The mechanism behind this ability was investigated in detail. It can be easily integrated and used to detect minute gas and fluid flows. Intricate flow details also can be monitored including flow speed, damping vibration, quasistatic force balance, and flow state. This is a cost-efficient, all-solution-based method that potentially can be applied for large-scale fabrication through the booming printing

Dr. Z. Liu, Dr. D. Qi, Dr. W. R. Leow, Dr. J. Yu, Dr. Y. Liu, Dr. B. Zhu, Y. Jiang, G. Chen, Prof. B. Liedberg, Prof. X. Chen
Innovative Centre for Flexible Devices (iFLEX)
School of Materials Science and Engineering
Nanyang Technological University
50 Nanyang Avenue, Singapore 639798, Singapore
E-mail: chenxd@ntu.edu.sg
M. Xiloyannnis, Dr. L. Cappello, Prof. L. Masia
School of Mechanical and Aerospace Engineering
Nanyang Technological University
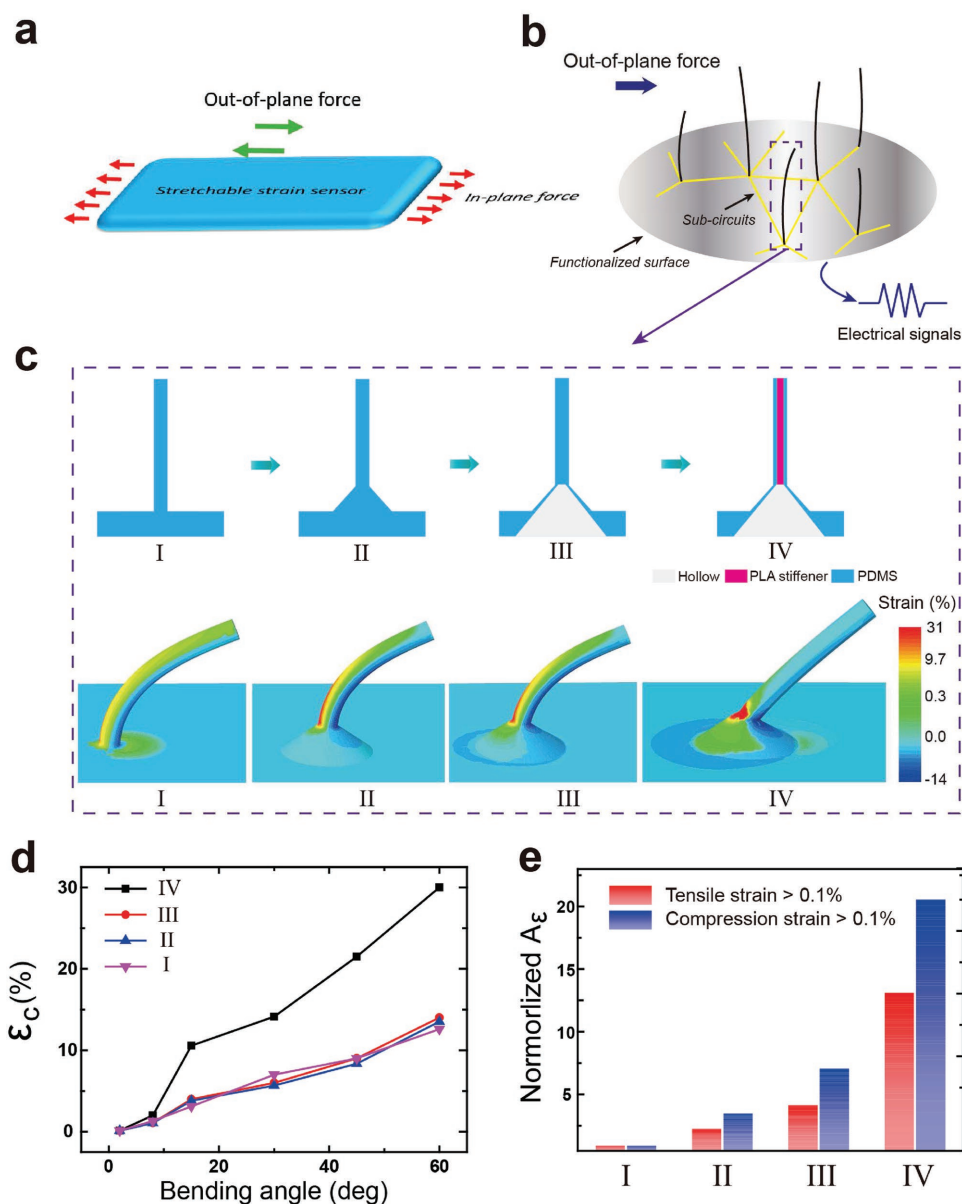50 Nanyang Avenue, Singapore 639798, Singapore

Figure 1. Mechanical design optimization of 3D-structured stretchable strain sensors. a) Diagram to show the in-plane force and out-of-plane force to be detected by a stretchable strain sensor. b) Diagram of the 3D-structured stretchable strain sensors to show the concept that this sensor could be integrated with the subcircuits for the functionalized surface, for example, soft robotics' skin, to detect the out-of-plane force. c) Three-step mechanical optimization based on energy conservation and classical bending moment theory and four structures (I, II, III, IV) developed correspondingly. The lower panel illustrates strain concentration and distribution under the bending angle of 45° as calculated by FEM simulation for the four different structures proposed. The negative value reflects compression. d) Strain concentration in the four different structures in a) under different bending angles. e) Strain distribution areas (>0.1%) in the four structures in (a) under the bending angle of 45°.

technology. We envision that our design could open up the development of 3D-structured stretchable sensors with superior properties for stretchable electronics.

For out-of-plane force detection, the key issue is to ensure efficient transduction of the force from the top of the sensor to the root, where the sensing unit is located and protected, in order to obtain high sensitivity. If the strain could not be properly transferred, the sensing performance would become worse. Therefore, the strain concentration at the root (ε_c) and the area of strain concentration (A_ε) should be optimized. We designed

four models of increasing complexity in terms of their 3D-architectured structures I–IV (Figure 1b,c) and determined the strain concentration and distribution for each model using finite element modeling (FEM) simulation. This approach was used to identify the key features of the 3D-structured stretchable strain sensor that contribute to signal amplification and transmission, and to define the optimal 3D design for strain detection.

For the most basic structure (Figure 1c, I), the sensor body was directly inserted into the elastic substrate and the whole substrate acted as a strain buffer zone that assists in absorbing

**ADVANCED
SCIENCE NEWS**

www.advancedsciencenews.com

**ADVANCED
MATERIALS**

www.advmat.de

the strain energy. For structure I, the strain was much less concentrated at the root where it was expected to induce significant local changes in both ε_c and A_ε (Figure 1c–e). It would limit the sensitivity of the 3D-structured stretchable strain sensor. Thus, first of all, we decided to tune the overall distribution volume of the strain by introducing a gradient transition region between the sensor body and the elastic substrate (Figure 1c, II). Such a region was beneficial in terms of avoiding sharp transitions. It also localized the strain rather than distributing it across the entire substrate. According to the classical formula of strain energy,[67] a relationship between the external work, W, and the inner deformation energy can be written as $W = \frac{1}{2}E\int_y \varepsilon^2 \, dV$, where E is the Young's modulus, ε is the strain induced, and V is the volume. By applying the mean-value theorem of integrals, this expression can be rewritten as $W = \frac{1}{2}E\overline{\varepsilon}^2 A_\varepsilon \overline{h}$, where $\overline{\varepsilon}$ is the midvalue, and $\overline{h}$ is the average thickness. Thus, for a given external work applied, A_ε can be maximized by relatively reducing the wall thickness of the volume, for example, by hollowing the gradient transition region (Figure 1c, III).

The FEM showed that although A_ε increased significantly by this two-step design (Figure 1e), ε_c did not increase for type I-III (Figure 1d). Again, we went back to the classical theory of bending moment.[67] In this theoretical model, the 3D-structured sensor can be simplified as an ideal beam, and the force acting on the root can be expressed as: $F = 3EI\gamma/l^3$, where γ is the deflection, E is the Young's modulus, l is the length of the sensor, and I is the moment of inertia. Thus, $\varepsilon_c \approx 3EI\gamma_{max}/l^3$ and then, for a specific sensor with a given length and applied γ_{max}, ε_c was determined by the stiffness, EI. The critical issue was how to enhance the stiffness of the sensor. In our design, a coaxial composite was used to increase the stiffness (Young's modulus) of the core. Thus, by replacing the core with a stiffer polymer, polylactic acid (PLA), whose modulus was larger than that of the surrounding soft polymer (polydimethylsiloxane), the stiffness would be increased and ε_c was enhanced (Figure 1c, IV). Finally, after this three-step design, the strain energy transfer from the top to the bottom was optimized and both A_ε and ε_c were enhanced (Figure 1d,e and Figure S2, Supporting Information). It should be emphasized, however, that further optimization following this procedure can be used to advance the performance of this 3D-structured stretchable strain sensor, for example, by adjusting the shape parameter of the conic root and modulus of the stiffener.

Having established the optimized structure for strain detection, our next challenge was how to deposit stretchable conducting film for strain measurement on this 3D structure. The stretchable conducting film must completely cover the out-of-plane gradient root region and part of the sensor body to enable accurate monitoring of the strain concentration at the root. Our previous study showed that single-wall carbon nanotubes (SWCNTs) modified with carboxyl groups could easily fully cover the in-plane flat substrate with SWCNTs thin film by utilizing a self-pinning approach.[68] Herein, we report the fabrication of self-pinned SWCNTs in the out-of-plane direction using a capillary force-mediated approach (**Figure 2**a). Specifically, after constructing the optimized structure through 3D printing, the SWCNTs solution was deposited at the root of the sensor and allowed to climb the sensor body (height of around 2 mm) through capillary action during which the self-pinning effect enabled the formation of an out-of-plane SWCNTs film (Figure S3, Supporting Information).

The unique feature of our method was that SWCNTs did not only form ring structure on the outside, but also fully covered the region between the rings with a thin film (Figure 2b). The method was also suitable for deposition on thin microwire of diameter ≈25 µm (Figure S4, Supporting Information) and could be applied to other polymer substrates, for example, Ecoflex.[69] Moreover, it was also found that multiple rings were formed on the sensor body (Figure 2a, Figures S5, S6 and Notes S1, S2, Supporting Information). Two major noncoplanar ring regions can be observed: one at the bottom of the sensor root and another one on the body, which can be used as connection points in the following encapsulation and testing process (Figure 2b). In order to show the advantage of this self-pinning method, we prepared a carbon nanotubes (CNT) and polydimethylsiloxane (PDMS) composited film, with CNT homogeneously dispersed in PDMS, and tested the sensing performance (Figure S7, Supporting Information). The result shows that the resistance change is much smaller (only ≈18%) and the repeatability is also poor, and our observation is consistent with previously reported results.[70]

The as-prepared 3D-structured stretchable strain sensor is presented in Figure 2b. As investigated before, the in-plane SWCNT film possesses full stretchability.[68] However, the stretchability of the SWCNT film in the out-of-plane direction in the sensing unit (in the root) had to be further studied. Here, it should be emphasized that a real fine hair on human body actually possesses the stretchable sensing unit (Figure S8, Supporting Information), so the stretchability should be achieved in order to fully mimic the function of the tactile hair. This stretchability is quite important for the sensor. It can guarantee the sensing capability of the sensor when suffering mechanical strain, including stretching, bending, and compressing. Previous reported hair-like sensors showed great potential in mimicking the function of bending strain sensing of tactile hairs,[60–66] however could not detect stretching strain and did not possess this important stretchable sensing unit which would make them be hard to integrate with other soft and stretchable sensing elements. To test the stretchability, the tensile strain was directly applied to the sensor body (Figure 2c) and the strain induced in the sensing unit was modeled by FEM (Figure 2d). The performance of the fabricated sensor was then tested with respect to its stretchability and strain-sensing function, especially for bending strain. The sensor (Figure 2c,d) displayed high stretchability (Figure 2e and Movies S1 and S2, Supporting Information). Moreover, it was able to detect and withstand at least 10 000 tensile strain cycles at 120% strain acting on the sensing unit (Figure 2f and Note S3, Supporting Information). It also showed excellent performance under compression strain (Figure S9a, Supporting Information). Therefore, this 3D-structured stretchable strain sensor can be used to detected tensile and compression strain. We also verified that a hollow root structure possessed significantly greater strain sensitivity compared to a solid root (Figure S9b, Supporting Information).

It would be highly desirable if a single 3D-structured stretchable strain sensor also could distinguish different strain directions, as it opens up for the exploration of complex flow patterns. According to the FEM simulation, it is obvious that the strain distribution in the root could be divided into four regions (Figure S2a, Supporting Information and inset of **Figure 3**a): i) tensile region, iii) compressed region, and ii,iv) two side
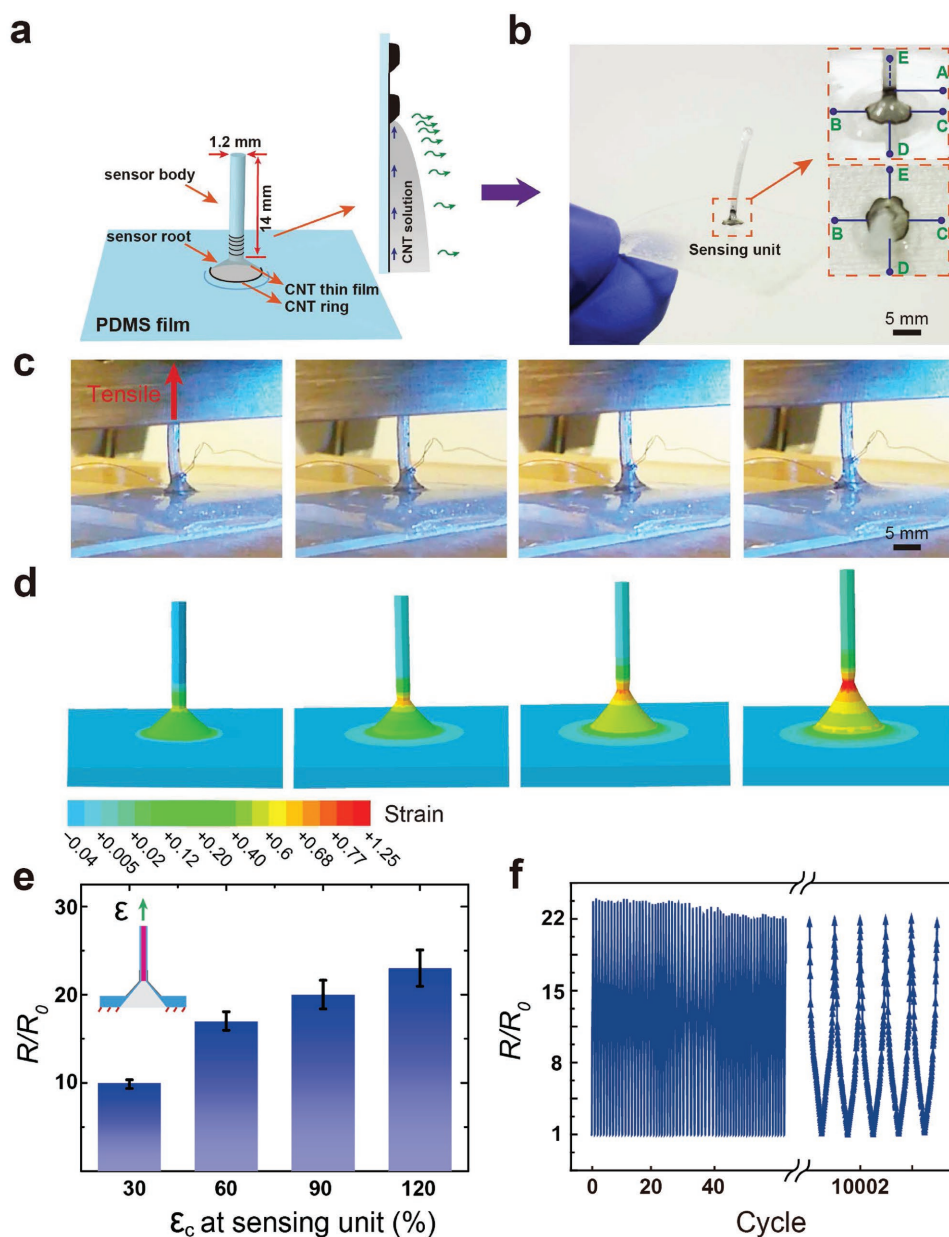
Figure 2. 3D-structured stretchable strain sensors with out-of-plane multirings by the 3D self-pinning effect and their performance with respect to strain sensing. a) Diagram of the slip-and-stick self-pinning effect which is essential for the formation of the out-of-plane multirings and CNT thin film on the sensor body. b) Image of a fabricated 3D-structured stretchable strain sensor. Inset illustrates the five-point encapsulation method. c) Optical images of the sensor during stretch and the corresponding strain distribution by FEM method shown in panel (d). e) Resistance change with different strain concentration applied to the sensing unit. Normalized resistance, R/R_0, where R and R_0 are the resistance values monitored with and without applied strain. The inset shows how the strain is applied. f) The durability of the sensor under tensile strain. Tensile strain of 120% at the sensing unit was applied for over 10 000 strain cycles.

regions. Thus, the strain direction can be recognized as long as regions i and iii are figured out. This can be accomplished by measuring the resistance between Point A on the sensor body and Points B, C, D, and E at the bottom ring (inset of Figure 2b and Figure S10, Supporting Information). When bending strain was applied in one direction, for example, from point B to point C, R_{AB} would increase with the bending angle due to the tensile strain, whereas R_{AC} would initially decrease and then change little. R_{AD} and R_{AE} changed marginally with increasing

bending angle. This pattern of changes was stable over a large number of cycles (Figure 3b) and enabled us to determine the strain direction. If the strain was applied in the direction in between BC or DE (Figure S11a, Supporting Information), the strain direction still can be determined. In this situation, R_{AB} and R_{AE} referred to the compression region and R_{AC} and R_{AD} to the tension region. For example, for bending angle of 15°, R_{AB} and R_{AE} decreased and R_{AC} and R_{AD} increased (Figure S11b–e and Note S4, Supporting Information). Therefore, the sloping

**ADVANCED
SCIENCE NEWS**

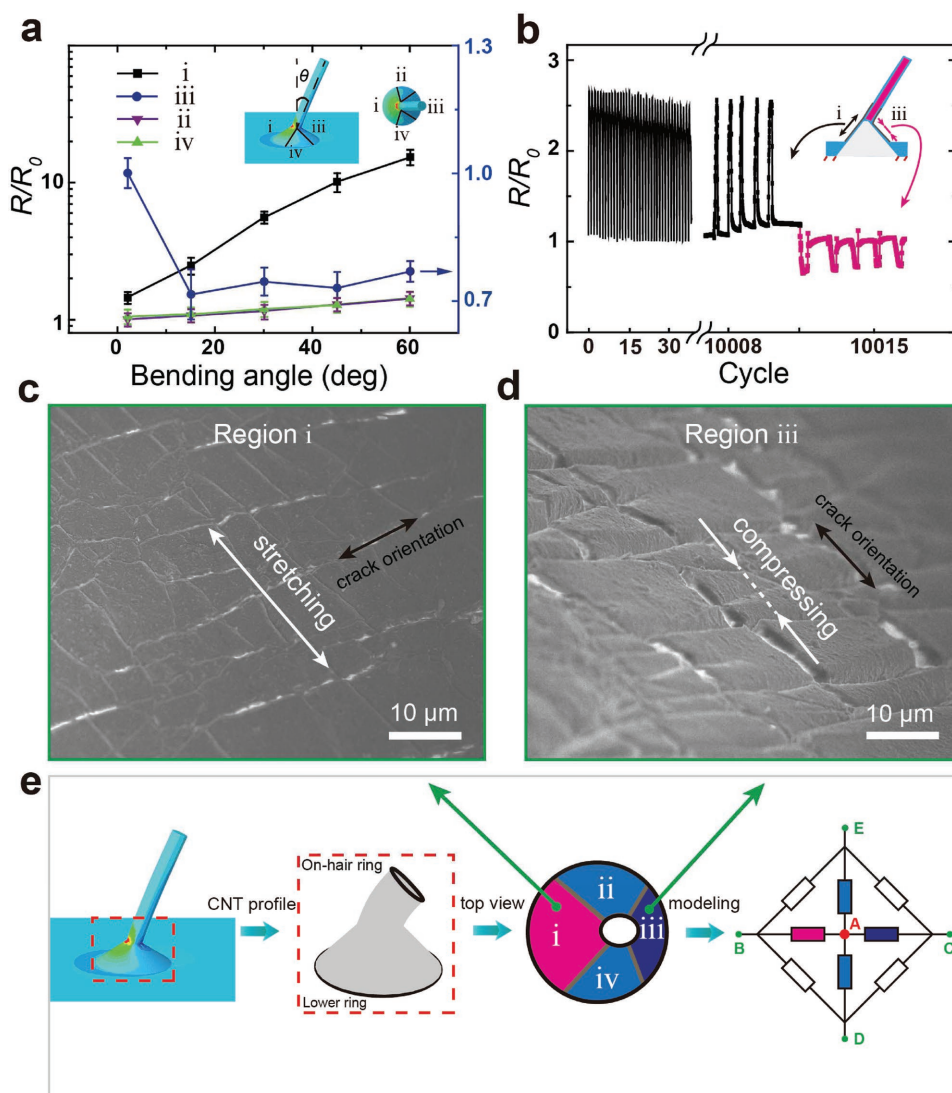www.advancedsciencenews.com

**ADVANCED
MATERIALS**

www.advmat.de

Figure 3. The resistance network modeling based on the strain distribution and related surface morphology under bending strain. a) Normalized resistance with different bending angle in different strain regions (as demonstrated in the inset). b) The durability of the sensor under bending strain. The inset presents the diagram of tensile strain and compression strain regions with black color and pink color, respectively. The compressive signal here was collected during the cycling and presented here at the end of the signal at region i. c,d) Cracks and wrinkles distribution in tensile region (region i) and compressed region (region iii) under the bending angle of 60°, respectively. White arrows indicate the stretching and compressing direction, respectively, and black one shows the crack orientation. e) The resistance network is abstracted through three-step modeling. The four regions correspond to that analyzed in Figure S2 (Supporting Information) and the four resistors in the final model.

direction also can be determined using the five-point method. Following our proposed strategy, the accuracy in determining the bending strain direction can most likely be improved further by increasing the connecting points on the lower ring.

To further understand the mechanism behind the resistance change, the surface morphology in the four regions was studied under bending strain of a single 3D-structured stretchable strain sensor. It can be seen that formation of cracks and wrinkles under strain differs significantly between the regions (Figure S12, Supporting Information). For instance, when bending strain was applied from point B to point C, the induced cracks aligned orthogonally to the stretching direction in region i (Figure 3c) resulting in an increase in resistance R_{AB}. Conversely, in the compression direction (region iii), the induced wrinkles

aligned orthogonally to the compression direction thereby shortening the conductive path, leading to a reduction in resistance R_{AC}. Moreover, the SWCNTs film can be modeled by a resistance network (Figure 3e and Note S5, Supporting Information). It can be seen that point A was vital for breaking the symmetry of the circuit, thus enabling us to determine the direction of the applied strain (Figure S13 and Note S6, Supporting Information).

The performance of the fabricated 3D-structured stretchable strain sensor under isotropic strain was also of importance for real applications as the sensor was inevitably exposed to multi-dimensional strains. To achieve isotropic stretchability was a nontrivial task that required a more complicated design. Our previous study has shown that the CNT film formed by self-pinning effect on the 2D flat substrate possessed isotropic

**ADVANCED
SCIENCE NEWS**

www.advancedsciencenews.com

**ADVANCED
MATERIALS**

www.advmat.de

stretchability.[68] Herein, we checked the isotropic stretchability of the sensor fabricated by 3D self-pinning. First, the 3D-structured stretchable strain sensor array was successfully fabricated (Figure S14a, Supporting Information). The two edges of the array were fixed on a hollowed rigid substrate. Then, we applied vertical stress from the bottom using a stick (Figure S14b, Supporting Information). The isotropic strain, ε_I, was estimated as A/A_0 _1, where A is the apparent area of the lower ring after applying isotropic strain and A_0 is its initial area. Under an applied isotropic strain of $\varepsilon_I = 50\%$ to the substrate, the bending strain was applied to the sensor body and the resistance was monitored in different strain domains. It was found that the overall trend of the resistance changes (R/R_0) remained

similar to the sample without isotropic strain applied (Figure 3a and Figure S14c, Supporting Information). This result revealed that the sensor array performs excellently under preexposure to isotropic strain. Moreover, it can be fully used to recognize the tactile pattern, for example, a tactile path with "NTU" shape (Figure S14d, Supporting Information). This ability of pattern recognition will be of importance for the e-skin and smart robots providing them with the ability to sense external stimuli without being in direct physical contact with the sensor system.

Finally, we demonstrated that the 3D-structured stretchable strain sensor (**Figure 4**a) can be employed for detection of gas and water flow at high sensitivity. When the sensor was subjected to light gas flow of 0.3-1.5 m/s (the weakest wind speed region
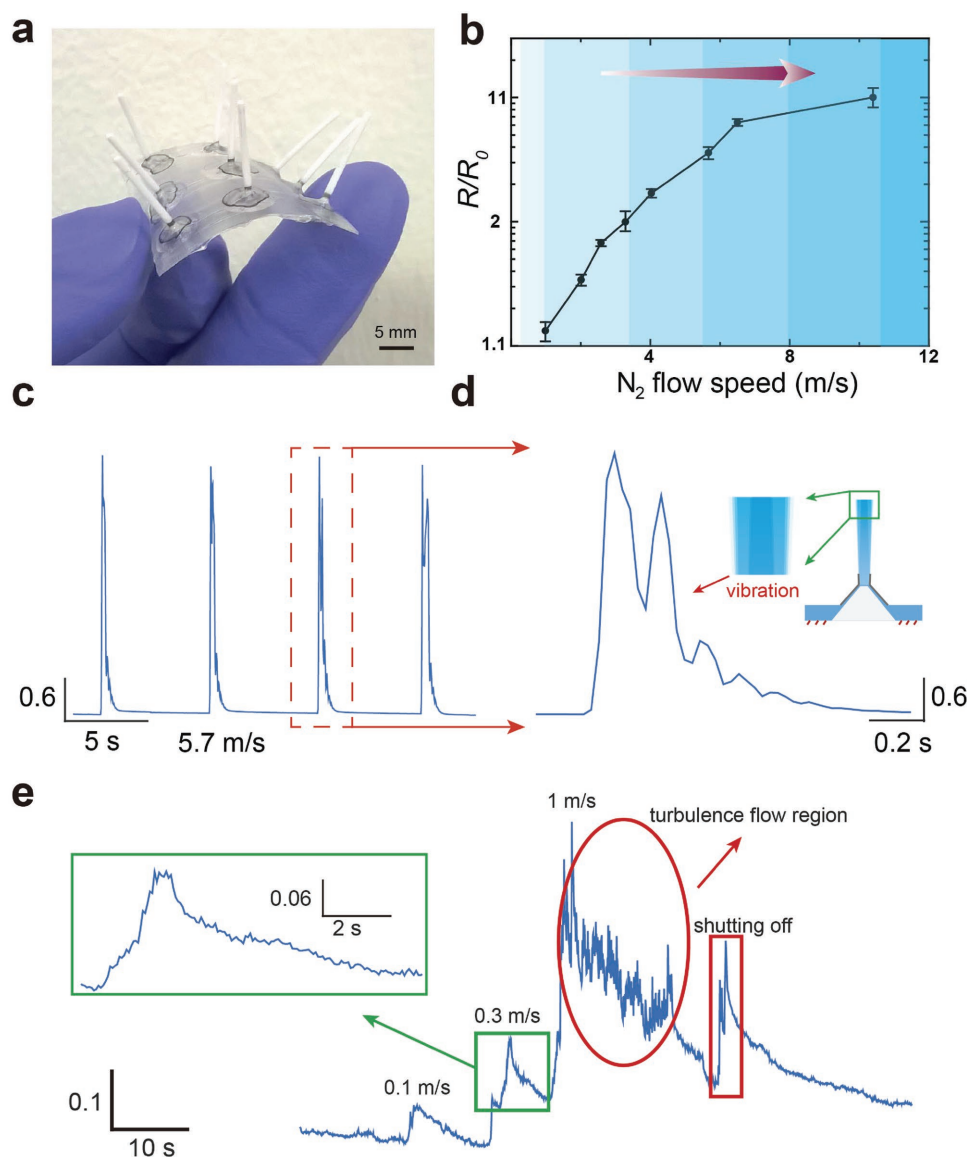

Figure 4. Isotropic stretchability of the sensor array and detection of subtle fluid flow. a) Photograph of the sensor array. b) Normalized resistance change under different speeds ranging from ≈1 to 11 m s^{-1}. c) Stability of the detection signals under the nitrogen speed of 5.7 m s^{-1}. d) Amplified view reveals that the damping vibration dominates the later part of the signal as illustrated in the inset. e) Signal obtained under different water speeds corresponding to two different flow states: laminar and turbulent flow. The green square indicates a typical signal of laminar flow and the inset shows the magnified view. The red ellipse highlights the typical vibration signal of the 3D-structured stretchable strain sensor induced by turbulent flow. The red rectangle shows the signal induced by the sudden shut-off of the water flow.

in which wind starts to be visible in smoke), a 20% change in resistance can be observed. For the region referred to as fresh breeze (8.0–10.7 m/s), the resistance increased by a factor of ≈10 (Figure 4b and Figure S15a, Supporting Information). More excitingly, even pulsed gas pressure for both low and high wind speed can be monitored through the damped vibrations of the sensor body (Figure 4c,d, Figure S16 and Note S7, Supporting Information). Water flow detection, on the other hand, occurred through static rather than vibration strain induced in the sensor root by the water pressure (Figure S15b, Supporting Information). This was because the viscosity of water is much larger than that of gases. It was interesting to note that the sensor can detect different flow states and even the shock induced by the fluid inertia due to sudden shut-off of water (Figure 4e and Note S8 and Movie S3, Supporting Information). This ability to sense the gas/fluid flow could benefit the wind/fluid field analysis during applications such as underwater robotics and flying control. Additionally, the size of the 3D-structruced stretchable strain sensor could be scaled down by more precise 3D printing technology to prepare the template. Since the carbon nanotube is very small, there is no barrier at the side of active materials to scale down. However, the wire bonding and encapsulation could be the barrier because the operational complexity would increase dramatically with the decrease of the size. This could be overcome by standardizing the manufacture process and arranging operation under the help of industrial robots. Also, for the further commercial product, 3D printing method could be replaced by the modular integration. The hair body with rigid core, the hollowed cone structure underneath, and the film substrate could be fabricated separately. Then, they are assembled together by proper soft glue, as long as the assembling process would not affect the original mechanical design to keep the effective strain transfer.

In summary, we reported a 3D-structured stretchable strain sensor which can detect tensile, compression, bending strains, and distinguish the strain direction by a single sensor. We also proposed a new strategy, capillary force-assisted 3D self-pinning of SWCNT into a thin film/ring structure, that utilized the combination of capillary rise and self-pinning. This enabled sensitive detection of subtle strains. It also offered us an avenue to distinguish the strain direction that was critical for many applications. The mechanism behind this ability was investigated and the key point was to break the symmetry of the resistance networks under the assistance of multi out-of-plane rings. It can be easily integrated and used to detect multistrains, minute gas, and fluid flows. Intricate flow details also can be monitored including flow speed, damping vibration, quasistatic force balance, and flow state. Additionally, it has to be emphasized that the 3D printing technology and solution-based material process employed herein make the whole process cost-efficient and attractive for large-scale applications. The concept of 3D-structured stretchable strain sensor and related design principles also open up for the exploration of new sensing principles for artificial electronic skin and stretchable electronics.

Experimental Section

Preparation of the Template and Stiffener: The template was 3D printed using Ultimaker 2 with the nozzle diameter of 0.4 mm and the printed polymer was PLA. The rigid part of PLA (around 15 mm in length) with the tensile modulus of 3.5 GPa was taken as the stiffener inside the sensor body. In order to make the sensor hollow, the template had a cone-shaped root with the diameter of 7 mm for the base circle and the height of 5 mm.

Preparation of 3D-Structured Stretchable Strain Sensor: The PDMS, purchased from Sigma-Aldrich, was employed as the soft substrate. The prepolymer and the cross linker were mixed together in a ratio of 10:1 by weight, and then defoamed by vacuum for about half of an hour, finally dropped onto the template fully, then spin coated at 500 rpm for 60 s and cured in 60 °C for 6 h. The thickness of the PDMS film was about 320 µm. The SWCNTs modified with the hydrophilic function group of carboxylic acid was from Carbon Solution, Inc. It was dispersed in the deionized water in ultrasound water bath. The power was 200 W for about 2 h (Fisher Scientific FB15051). The SWCNTs with the concentration of 2 g L^{-1} was well dispersed in the solution and ready to be used after around 15 min' standing for the subsiding of the large aggregates.

Next, the gradient root of the sensor was exposed to the oxygen plasma to become hydrophilic by using a covering mask with circled hollow pattern to limit the hydrophilic area. The oxygen pressure was 5 mbar with power of 50 W for 0.5 min. After removing the hollow mask, 10 µL SWCNT solution was dropped on the gradient root and immediately covered the pattern even climbing up the sensor body to the height of about 2 mm under the assistance of capillary force. After the evaporation for around 30 min in the air at room temperature, the 3D self-pinning effect ended. Finally, the sensor was cut off from the PLA substrate with the stick left inside the sensor body, and the 3D-structured stretchable strain sensor was ready to be tested after the careful encapsulation. The sensor array was also prepared in this similar method. However, the wire bonding was more complicated and performed among the sensors following the pattern of crossing bar, and then the resistance vibration of certain sensor was calculated by solving the linear equations.

Preparation of CNT&PDMS Composite Film: Multiwall CNTs (Timesnano, Chengdu, China) were with 30–50 nm in diameter and 10–20 µm in length. The CNT powder was dispersed in toluene at an 8 wt% concentration in sonicated bath. PDMS monomer was added to the mixture followed by a full mixing and the cross linker was added after the full evaporation of the toluene. Then, the air bubble was removed by vacuum. Finally, the mixture was poured to the petri dish and cured for more than 2 d at room temperature.

Wire Bonding and Dynamic Resistance Testing under Cyclic Loading: The bonding copper wires were with diameter of 0.1 mm to make the compliant contact with the SWCNTs rings (Figure S9, Supporting Information). The liquid metal (Gallium–Indium eutectic, Sigma-Aldrich) severed as the conductive adhesive for hugely improving the stability of this encapsulation, especially benefitting the dynamic resistance testing. It should be emphasized that wires were all shaped in an arc to keep continuous contact during the cyclic loading.

Characterization: The cyclic bending strain was also applied by using this machine and a customized transducer to change the vertical displacement to rotation. Field emission scanning electron microscopy was performed using JEOL 7600F with the accelerating voltage of 5 kV and the current of 110 pA. The resistance was measured by using Keithley 4200-SCS with the sampling rate of 125 points per second. The testing process of tensile strain was also illustrated in Movie S1 (Supporting Information).

Detection of Gas and Water Flow: Nitrogen was employed here to apply the gas flow of different speed. The double faced adhesive tape was used to modify on the head of the sensor body to enhance the gas pressure receiving. Gas gun was open first, applied nitrogen for around 1 s, and then removed. The sensor would suffer the damping vibration process before reaching to the static state at last. The rubber tube with diameter of 5 mm was utilized to tune the different flow state by adjusting the tap pressure. Additionally, Reynolds number is the standard dimensionless number reflecting the flow state, and when it is larger than 4000, the flow state is usually taken as turbulence.

**ADVANCED
SCIENCE NEWS**

www.advancedsciencenews.com

**ADVANCED
MATERIALS**

www.advmat.de

Conflict of Interest

The authors declare no conflict of interest.

Keywords

[1] B. Tee, C. Wang, R. Allen, Z. Bao, *Nat. Nanotechnol.* **2012**, *7*, 825.
[2] B. Zhu, H. Wang, Y. Liu, D. Qi, Z. Liu, H. Wang, J. Yu, M. Sherburne, Z. Wang, X. Chen, *Adv. Mater.* **2016**, *28*, 1559.
[3] J. J. Boland *Nat. Mater.* **2010**, *9*, 790.
[4] D. Rus, M. T. Tolley, *Nature* **2015**, *521*, 467.
[5] T. J. White, D. J. Broer, *Nat. Mater.* **2015**, *14*, 1087.
[6] M. A. McEvoy, N. Correll, *Science* **2015**, *347*, 70.
[7] H. Wang, Y. Du, Y. Li, B. Zhu, W. R. Leow, Y. Li, J. Pan, T. Wu, X. Chen, *Adv. Funct. Mater.* **2015**, *25*, 3825.
[8] T. Sekitani, U. Zschieschang, H. Klauk, T. Someya, *Nat. Mater.* **2009**, *8*, 494.
[9] U. G. K. Wegst, H. Bai, E. Saiz, A. P. Tomsia, R. O. Ritchie, *Nat. Mater.* **2015**, *14*, 23.
[10] B. Zhu, Z. Niu, H. Wang, W. R. Leow, H. Wang, Y. Li, L. Zheng, J. Wei, F. Huo, X. Chen, *Small* **2014**, *10*, 3625.
[11] H. Lee, T. K. Choi, Y. B. Lee, H. R. Cho, R. Ghaffari, L. Wang, H. J. Choi, T. D. Chung, N. Lu, T. Hyeon, S. H. Choi, D.-H. Kim, *Nat. Nanotechol.* **2016**, *11*, 566.
[12] J. Liang, L. Li, D. Chen, T. Hajagos, Z. Ren, S. Chou, W. Hu, Q. Pei *Nat. Commun.* **2015**, *6*, 7647.
[13] X. Wang, Y. Gu, Z. Xiong, Z. Cui, T. Zhang, *Adv. Mater.* **2014**, *26*, 1309.
[14] M. Zarek, M. Layani, I. Cooperstein, E. Sachyani, D. Cohn, S. Magdassi, *Adv. Mater.* **2016**, *28*, 4449.
[15] Y. Zang, F. Zhang, D. Huang, C. Di, D. Zhu, *Adv. Mater.* **2015**, *27*, 7979.
[16] X. Chen, *Small Methods* **2017**, *1*, 1600029.
[17] J. T. Muth, D. M. Vogt, R. L. Truby, Y. Mengüç, D. B. Kolesky, R. J. Wood, J. A. Lewis, *Adv Mater.* **2014**, *26*, 6307.
[18] M. Amjadi, K. U. Kyung, I. Park, M. Sitti, *Adv. Funct. Mater.* **2016**, *26*, 1678.
[19] S.-H. Bae, Y. Lee, B. K. Sharma, H.-J. Lee, J.-H. Kim, J.-H. Ahn, *Carbon* **2013**, *51*, 236.
[20] J. J. Park, W. J. Hyun, S. C. Mun, Y. T. Park, O. O. Park, *ACS Appl. Mater. Interfaces* **2015**, *7*, 6317.
[21] M. Amjadi, M. Turan, C. P. Clementson, M. Sitti, *ACS Appl. Mater. Interfaces* **2016**, *8*, 5618.
[22] S. Cheng, Z. Wu, *Adv. Funct. Mater.* **2011**, *21*, 2282.
[23] E. Roh, B.-U. Hwang, D. Kim, B.-Y. Kim, N.-E. Lee, *ACS Nano* **2015**, *9*, 6252.
[24] J. Kim, M. Lee, H. J. Shim, R. Ghaffari, H. R. Cho, D. Son, Y. H. Jung, M. Soh, C. Choi, S. Jung, *Nat. Commun.* **2014**, *5*, 5747.
[25] X. Liao, Q. Liao, X. Yan, Q. Liang, H. Si, M. Li, H. Wu, S. Cao, Y. Zhang, *Adv. Funct. Mater.* **2015**, *25*, 2395.
[26] C. Pang, G.-Y. Lee, T.-I. Kim, S. M. Kim, H. N. Kim, S.-H. Ahn, K.-Y. Suh, *Nat. Mater.* **2012**, *11*, 795.
[27] S. Chen, Y. Wei, X. Yuan, Y. Lin, L. Liu, *J. Mater. Chem. C* **2016**, *4*, 4304.
[28] A. Frutiger, J. T. Muth, D. M. Vogt, Y. Mengüç, A. Campo, A. D. Valentine, C. J. Walsh, J. A. Lewis, *Adv. Mater.* **2015**, *27*, 2440.
[29] D. Son, J. Lee, S. Qiao, R. Ghaffari, J. Kim, J. E. Lee, C. Song, S. J. Kim, D. J. Lee, S. W. Jun, *Nat. Nanotechnol.* **2014**, *9*, 397.
[30] Y. Cheng, R. Wang, J. Sun, L. Gao, *Adv. Mater.* **2015**, *27*, 7365.
[31] R. Rahimi, M. Ochoa, W. Yu, B. Ziaie, *ACS Appl. Mater. Interfaces* **2015**, *7*, 4463.
[32] N. Lu, C. Lu, S. Yang, J. Rogers, *Adv. Funct. Mater.* **2012**, *22*, 4044.
[33] X. Wang, T. Li, J. Adams, J. Yang, *J. Mater. Chem. A* **2013**, *1*, 3580.
[34] J. Shi, X. Li, H. Cheng, Z. Liu, L. Zhao, T. Yang, Z. Dai, Z. Cheng, E. Shi, L. Yang, *Adv. Funct. Mater.* **2016**, *26*, 2078.
[35] S. Gong, D. T. Lai, B. Su, K. J. Si, Z. Ma, L. W. Yap, P. Guo, W. Cheng, *Adv. Electron. Mater.* **2015**, *1*, 1400063.
[36] X. Liao, Z. Zhang, Z. Kang, F. Gao, Q. Liao, Y. Zhang, *Mater. Horiz.* **2017**, *4*, 502.
[37] B. Yin, Y. Wen, T. Hong, Z. Xie, G. Yuan, Q. Ji, H. Jia, *ACS Appl. Mater.Interfaces* **2017**, *9*, 32054.
[38] C. Wang, X. Li, E. Gao, M. Jian, K. Xia, Q. Wang, Z. Xu, T. Ren, Y. Zhang, *Adv. Mater.* **2016**, *28*, 6640.
[39] Q. Li, Z. Ullah, W. Li, Y. Guo, J. Xu, R. Wang, Q. Zeng, M. Chen, C. Liu, L. Liu, *Small* **2016**, *12*, 5058.
[40] S. Chen, Y. Wei, S. Wei, Y. Lin, L. Liu, *ACS Appl. Mater. Interfaces* **2016**, *8*, 25563.
[41] G. Cai, J. Wang, K. Qian, J. Chen, S. Li, P. S. Lee, *Adv. Sci.* **2017**, *4*, 1600190.
[42] Z. Ma, B. Su, S. Gong, Y. Wang, L. W. Yap, G. P. Simon, W. Cheng, *ACS Sensors* **2016**, *1*, 303.
[43] Y. Hu, T. Zhao, P. Zhu, Y. Zhu, X. Shuai, X. Liang, R. Sun, D. D. Lu, C.-P. Wong, *J. Mater. Chem. C* **2016**, *4*, 5839.
[44] H. Yang, D. Qi, Z. Liu, B. K. Chandran, T. Wang, J. Yu, X. Chen, *Adv. Mater.* **2016**, *28*, 9175.
[45] A. Atalay, V. Sanchez, O. Atalay, D. M. Vogt, F. Haufe, R. J. Wood, C. J. Walsh, *Adv. Mater. Technol.* **2017**, *9*, 1700136.
[46] T. Lee, Y. W. Choi, G. Lee, P. V. Pikhitsa, D. Kang, S. M. Kim, M. Choi, *J. Mater. Chem. C* **2016**, *4*, 9947.
[47] J. Zhou, H. Yu, X. Xu, F. Han, G. Lubineau, *ACS Appl. Mater. Interfaces* **2017**, *9*, 4835.
[48] Y. He, Q. Gui, S. Liao, H. Jia, Y. Wang, *Adv. Mater. Technol.* **2016**, *1*, 1600170.
[49] D. Qi, Z. Liu, W. R. Leow, X. Chen, *MRS Bull.* **2017**, *42*, 103.
[50] X.-G. Yu, Y.-Q. Li, W.-B. Zhu, P. Huang, T.-T. Wang, N. Hu, S.-Y. Fu, *Nanoscale* **2017**, *9*, 6680.
[51] Z. Liu, X. Wang, Q. Qi, C. Xu, J. Yu, Y. Liu, Y. Jiang, B. Liedberg, X. Chen, *Adv. Mater.* **2017**, *27*, 1603382.
[52] Y. Liu, K. He, G. Chen, W. R. Leow, X. Chen, *Chem. Rev.* **2017**, *117*, 12893.
[53] T. F. O'Connor, M. E. Fach, R. Miller, S. E. Root, P. P. Mercier, D. J. Lipomi, *PloS One* **2017**, *12*, e0179766.
[54] F. G. Barth, J. A. Humphrey, T. W. Secomb, *Sensors and Sensing in Biology and Engineering*, Springer Press, New York, USA **2012**.
[55] N. A. Monteiro-Riviere, *Toxicology of the Skin*, CRC Press, Boca Raton, FL, USA **2010**.
[56] Z. Halata, *J. Invest. Dermatol.* **1993**, *101*, 75S.

[57] K. Takei, Z. Yu, M. Zheng, H. Ota, T. Takahashi, A. Javey, *Proc. Natl. Acad. Sci. USA* **2014**, *111*, 1703.

[58] S. Harada, W. Honda, T. Arie, S. Akita, K. Takei, *ACS Nano* **2014**, *8*, 3921.

[59] A. Alfadhel, J. Kosel, *Adv. Mater.* **2015**, *27*, 7888.

[60] N. Chen, C. Tucker, J. M. Engel, Y. Yang, S. Pandya, C. Liu, *J. Microelectromech. Syst.* **2007**, *16*, 999.

[61] J. M. Engel, J. Chen, C. Liu, D. Bullen, *J. Microelectromech. Syst.* **2006**, *15*, 729.

[62] C. Liu, *Bioinsp. Biomim.* **2007**, *2*, S162.

[63] J.-E. Han, D. Kim, K.-S. Yun, *Sens. Actuators, A* **2012**, *188*, 89.

[64] K. Slinker, M. R. Maschmann, C. Kondash, B. Severin, D. Philips, B. T. Dickinson, G. Reich, J. Baur, *Proc. SPIE* **2015**, *9429*, 942917.

[65] M. R. Maschmann, G. J. Ehlert, B. T. Dickinson, D. M. Phillips, C. W. Ray, G. W. Reich, J. W. Baur, *Adv. Mater.* **2014**, *26*, 3230.

[66] A. G. P. Kottapalli, M. Bora, E. Kanhere, M. Asadnia, J. Miao, M. S. Triantafyllou, *Sensors* **2017**, *17*, 1728.

[67] A. Öchsner, *Continuum Damage and Fracture mechanics*, Springer, Singapore **2015**.

[68] Z. Liu, D. Qi, P. Guo, Y. Liu, B. Zhu, H. Yang, Y. Liu, B. Li, C. Zhang, J. Yu, B. Liedberg, X. Chen, *Adv. Mater.* **2015**, *27*, 6230.

[69] Z. Lv, Y. Luo, Y. Tang, J. Wei, Z. Zhu, X. Zhou, W. Li, Y. Zeng, W. Zhang, Y. Zhang, D. Qi, S. Pan, X.J. Loh, X. Chen, *Adv. Mater.* **2018**, *30*. 1704531.

[70] M. Manzoor, P. Lemoine, D. Dixon, J. Hamilton, P. Maguire, *AIP Adv.* **2015**, *5*, 107237.